The Early Upper Paleolithic deposit of Mughr el-Hamamah (Jordan): Archaeobotanical taphonomy and site formation processes

Mónica Alonso-Eguiluz[1, *], Michael B. Toffolo[2,3], Chantel E. White[4], Eleni Asouti[5], Elisabetta Boaretto[6], Liv Nilsson Stutz[7], Aaron Stutz[8] and Rosa María Albert[9,10]

[1] Archaeology, Environmental Changes and Geo-Chemistry (AMGC). Vrije Universiteit Brussel, Belgium

[2] Geochronology and Geology Program. Centro Nacional de Investigación sobre la Evolución Humana (CENIEH), Spain

[3] Archéosciences Bordeaux, UMR 6034 CNRS. Université Bordeaux Montaigne, France

[4] Center for the Analysis of Archaeological Materials. University of Pennsylvania Museum of Archaeology and Anthropology, United States

[5] Department of Archaeology, Classics and Egyptology. University of Liverpool, United Kingdom

[6] Scientific Archaeological Unit, Kimmel Center for Archaeological Science. Weizmann Institute of Science, Israel

[7] Department of Cultural Sciences. Linnaeus University, Sweden

[8] Bohusläns Museum, Sweden

[9] Department of Prehistory. Autonomous University of Barcelona, Spain

[10] ICREA, Pg. Lluis Companys, 23, Barcelona, Spain

*Corresponding author: monica.alonso.eguiluz@vub.be
Department of Art Studies and Archaeology
Faculty of Arts and Philosophy
Building C - Room 5.22
Pleinlaan 2
1050 Brussel
Belgium

ABSTRACT

With a rich, well-dated Early Upper Palaeolithic layer, the Mughr el-Hamamah cave site is key for understanding the Middle-Upper Palaeolithic transition in the Levant. The archaeological deposit consists of two units. Layer A resulted from pastoral activities during the 20th century and Layer B dated between 44.5-40.0 ky BP. During Layer A's formation, shepherds disturbed Layer B, redepositing Early Upper Palaeolithic sediments and lithic artefacts in Layer A matrix. Activity from Layer A's formation also resulted in spatially patchy percolation and bioturbation, leaving microarchaeological traces such as dung spherulites in some areas in Layer B. In contrast, contemporaneous chemical diagenetic processes from Layer B's primary formation caused spatially uneven post-depositional dissolution of animal bone. In this article we present a multi-proxy microarchaeological approach to investigate the post-depositional processes in Layer B, focussing on possible impacts on the plant archaeological record. The identification of intrusive spherulites from shepherds' activities define the limits of disturbance in Layer B. Micromorphological analyses have identified four intact micro-facies in Layer B, representing an interplay of natural and anthropogenic factors. Micromorphological details in bedded combustion features favour the interpretation that associated phytoliths represent fuel traces. Dicot fruit phytoliths occur in the western area of the cave, where well-preserved charred wood and seeds were also found. Grass-diagnostic phytoliths correspond to C_3 and C_4 taxa, indicating an overall humid environment with dry spells. Microarchaeological analysis identifies traces of both bedded and dispersed hearth materials, mixed with variable plant resources for

food, fuel, and possibly other uses. This strengthens the interpretation of Mughr el-Hamamah Layer B as a dense, complicated palimpsest of recurring activities, formed over many millennia.

keywords: Early Upper Palaeolithic; Post-depositional processes; Micromorphology; Phytoliths; FTIR; Spherulites; Cave archaeology

1. Introduction

Mughr el-Hamamah (hereafter MHM) is located in the Ajlun Governorate (Jordan) (Fig. 1), in an ecotone between the wetland and steppe vegetation of Lake Lisan and the Mediterranean forest of the Jordanian plateau (Stutz and Nilsson Stutz, 2017). The main cave preserves an archaeological deposit with unconformably superposed layers A and B. Layer A derives from 20th century shepherd activities along with some redeposited Early Upper Palaeolithic (EUP) artefacts. The underlying Layer B contains a rich EUP archaeological record with abundant zooarchaeological remains, charred seeds and charred wood, lithic artefacts, and some isolated hominin remains (Stutz et al., 2015). Macrobotanical analyses from flotation samples at MHM are currently in preparation for publication. The site has been dated with radiocarbon assays on ABOx-pretreated wood charcoal samples, indicating an occupation concentrated between 44.5-40.0 ky BP (Fig. 3, Table 1). MHM is notably the sole EUP cave site excavated in the Jordan Valley, since Emireh Cave was investigated in the 1920’s (Shea et al., 2019; Stutz et al., 2015; Stutz and Nilsson Stutz, 2017).

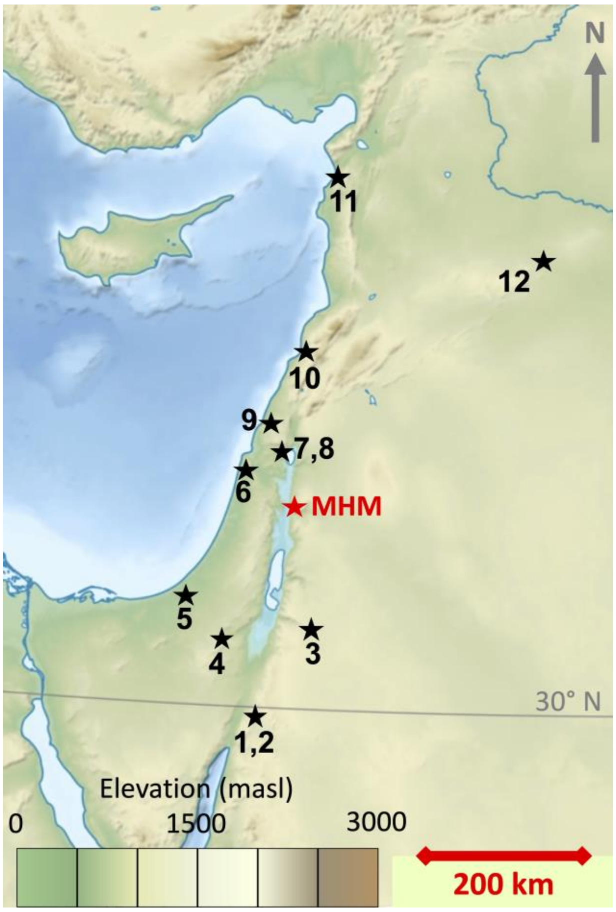

Fig. 1. Map of the Levant marked with important Late Middle Palaeolithic (LMP, ca. 70-48 ka) and earliest Upper Palaeolithic (EUP, circa 47-40 ka) sites. MHM-Mughr el-Hamamah; 1 & 2-Tor Faraj (LMP) and Tor Fawwaz (EUP); 3-Tor Sadaf (EUP); 4-Boker Tachtit (EUP); 5-Far'ah II (LMP); 6-Kebara Cave (LMP-EUP); 7 &

8 - Amud Cave (LMP) and Emireh Cave (LMP-EUP); 9-Manot Cave (EUP); 10-Ksar Akil Rockshelter (LMP-EUP); 11-Üçağızlı Cave (EUP); 12-Umm el-Tlel (LMP-EUP). Basemap by user Fulvio314 on it.wikipedia.org, available on Wikimedia. Commons under a CC.3.0. Unported. License

Despite the apparent good preservation of the archaeological assemblage in Layer B, field observations noted some modern-era disturbances related to the later occupation of the cave by shepherds during the 20th century (Fig. 2). Modern alterations of cave deposits caused by shepherds are common, and they have been reported in several studies (i.e., Kehl et al, 2016; Kadowaki et al. 2021). This disturbance also called into question the reliability of the presence of plant microremains (phytoliths) in the EUP levels and their possible origin from the shepherd's activities. Other observations were made relating to the uneven preservation of the organic remains. For example, bone appeared to be better preserved in the eastern area while charred plant remains were better preserved in the western area of the cave. Hence, to correctly understand the activities and use of plants in the cave by EUP occupants, it is essential to clarify the post-depositional processes affecting the archaeological deposits and assess the degree to which shepherds disturbed the archaeological record of Layer B.

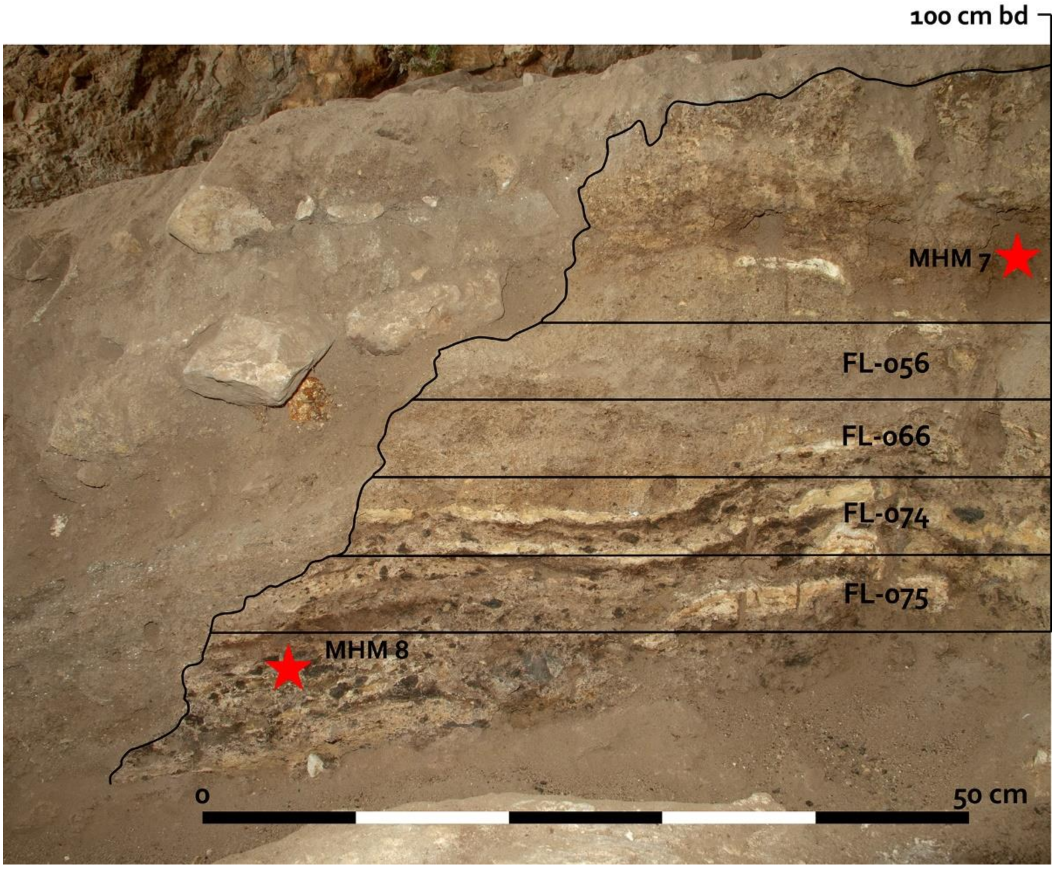

Fig. 2. Western section of square B2. Irregular solid line shows the cut into Early Upper Palaeolithic Layer B, with the overlying recent Layer A. The stars mark the west-east and vertical coordinates of carbonized wood radiocarbon samples MHM7 and 8. The flotation (FL) samples mark the arbitrary 5 cm levels of in situ layer B material sampled in the adjacent (within-the-section) subsquare B1b, which yielded some of the carbonized wild legume seeds and pistachio shell fragments described in the text. Micromorphology sample 3 is from square B2a, directly in front of the section through the bedded hearth features visible in the photograph. This sample captures bedded combustion material interstratified with a silt component (see text). As in typical complicated, diagenetically altered Pleistocene cave deposits, it was not possible to follow individual combustion features laterally. Thus, carbonized botanical material the stratified combustion features were sampled in FL-066, 074 and 075, in order to obtain a macrobotanical sequence over a relatively well-preserved portion of the Layer B deposits.

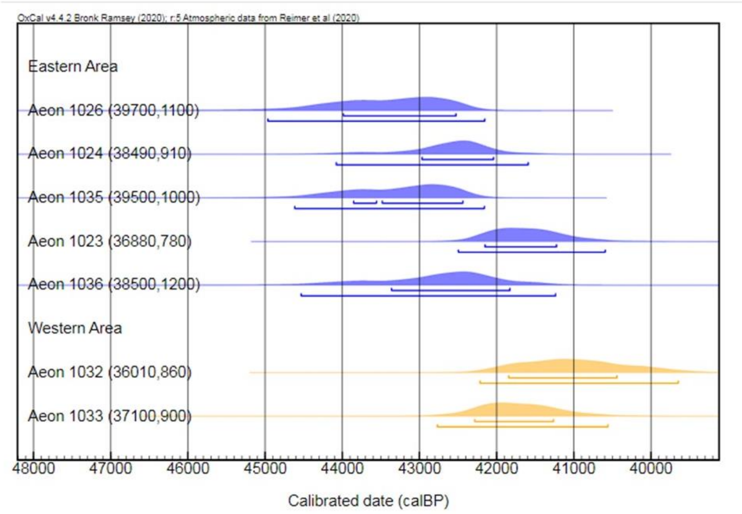

Fig. 3. Probability distribution function of the calibrated dates from Table 1 In blue dates related to samples from the Eastern Area and in orange the samples from the Western Area.

	MHM #	Sub-square	East coord.	South coord.	Depth (BD)	Comment	Lab Number	ABOx Comb. T °C	^{14}C Age ± 1σ year BP	C %	Calibrated range ±1σ year BP	Calibrated range ±2σ year BP
Eastern area main deposits	MHM 5-325	B5c	5	61	112	under limestone	Aeon 1026	625	39700 ± 1100	38.6	43000 - 42500	45000 - 42150
	MHM 4	C5a	22	18	124	under Hearth 1	Aeon 1024	325	38490 ± 910	54.3	43000 - 42000	44100 - 41550
	MHM 10-325	B5d	55	85	129	under limestone with bone and flint	Aeon 1035	325	39500 ± 1000	55.3	43900 (11.9%) 43550 43500 (56.4%) 42400	44650 - 42150
	MHM 2	C5a	23	40	131.5	under Hearth 2	Aeon 1023	325	36880 ± 780	53.8	42150 - 41200	42500 - 40550
	MHM 11	C5a	6	34	134.5		Aeon 1036	325	38500 ± 1200	55.1	43400 - 41800	44550 - 41200
Western area	MHM 7	B2a	0	0	117	in phosphatised upper layer B	Aeon 1032	325	36010 ± 860	50.9	41850 - 40400	42250 - 39600
	MHM 8	B2d	90	57	141	from hearth layers under rock	Aeon 1033	325	37100 ± 900	52.9	42300 - 41250	42800 - 40550

Table 1. Radiocarbon dates of MHM site. Non identified wood charcoal samples were processed applying ABOx procedure. Temperature for combustion is given in the table (ABOx Comb. T °C). Calibrated ranges are rounded to nearest 50y. Calibrated ages were obtained using the calibration program OxCal v4.4.5 Bronk Ramsey (2020) and with the atmospheric calibration curve of Reimer et al. (2020).

Bearing in mind the complexity and different origins (natural and anthropogenic) of the post-depositional processes, it is key to apply a multi-proxy approach to reconstruct the biography of the deposit, as well as the state of preservation of the different archaeological traces. Microarchaeology provides the tools to achieve this purpose, as it studies the invisible record that makes up the macroarchaeological record and the sedimentary matrix in which it is buried. Microarchaeology groups several high-resolution techniques, such as micromorphology, which sometimes requires specific extraction methods (Weiner, 2010). The combination of different high-resolution techniques provides important information from many different perspectives. This allows us to reconstruct the processes that led to the formation of the archaeological deposit and the plant-related activities that took place at the site.

To understand the post-depositional processes at MHM Layer B and the state of preservation of the archaeological record (macro and micro), we used a microarchaeological multi-proxy approach, which included micromorphology, Fourier Transformed Infrared Spectroscopy (FTIR), phytoliths and faecal spherulites analyses.

2. Materials and Methods

2.1 Micromorphology

Blocks of intact sediments (n=14) (Fig. 4) were collected for micromorphological analysis with the aim of understanding the formation and post-depositional processes of specific contexts (e.g., combustion features). The blocks were jacketed in plaster for transport to the Boston University Microstratigraphy Laboratory where they were embedded in a mixture of polyester resin and acetone (ratio 70:30). Hardened blocks were sliced with a rock saw to obtain 8x6 cm chips, which were processed into thin section (30 µm thickness). Thin sections (n=21) were analysed using a petrographic microscope (magnifications 25x, 50x, 100x, 200x, 400x). Micromorphological descriptions are based on established literature (Macphail and Goldberg, 2017; Nicosia and Stoops, 2017; Stoops, 2021; Stoops et al., 2018). Considering that similar depositional units occur repeatedly throughout the sampled contexts, we grouped micromorphology samples under different microfacies types (MFT), according to the description given by Flügel (2004: 1): "the total of all sedimentological and paleontological data which can be described and classified from thin sections, peels, polished slabs or rock samples". This choice was dictated by the aim of understanding the post-depositional processes in terms of lithological units (e.g., Layer A and Layer B at the macroscopic scale of observation) and location within the cave (east vs. west), rather than systematically sample and describe all micro-contexts from an anthropogenic perspective. In doing so, we followed previous micromorphological studies of cave sites (Goldberg et al., 2009, 2015).

2.2 FTIR

68 bulk sediment samples were analysed using FTIR, which provides a quantitative assessment of the gross mineral composition of sediments. FTIR helps us to better understand the diagenetic processes that may have altered some of the archaeological remains. Seven samples were collected from Layer A, 58 from Layer B, 1 from the surface (sample C9), and two that could not be securely related to Layers A or B (samples F5 and F2) (Fig. 4). Samples were collected from grid squares A1, A2, B2 and B3 located on the western area inside the cave; squares B4, B5, and C5 in the eastern area inside the cave, and finally from squares F2, F3 and F4, representing a 1x3m sounding just inside the dripline of the cave (Fig. 4). Additionally, samples from squares A1 and A2 were prioritised due to the good associated preservation of charred plant remains (seeds).

The methods used follow those of Weiner (2010). Tens of micrograms of archaeological sediment were homogenised with KBr to obtain the pellets. Infrared spectra were obtained in transmission mode using a Nicolet iS5 spectrometer at 4 cm^{-1} resolution and in 32 scans in the 4000-400 cm^{-1} spectral range. To assess the origin of calcite, when present, we applied the infrared grinding curve method developed by Regev et al. (2010) based on the measurement of the ν_2 and ν_4 intensity (874 and 713 cm^{-1}, respectively) normalised to the ν_3 intensity (1420 cm^{-1}). Normalised intensity values were compared with reference grinding curves published in Regev et al. (2010). Band shifts of clay minerals exposed to elevated temperatures, described by Berna et al. (2007), were used to determine the possible thermal alteration of clay minerals in the sediments. Additionally, the FTIR reference collection of standard materials provided by the Kimmel Center of Archaeological Science, Weizmann Institute of Science was consulted (http://www.weizmann.ac.il/kimmel-arch/infrared-spectra-library).

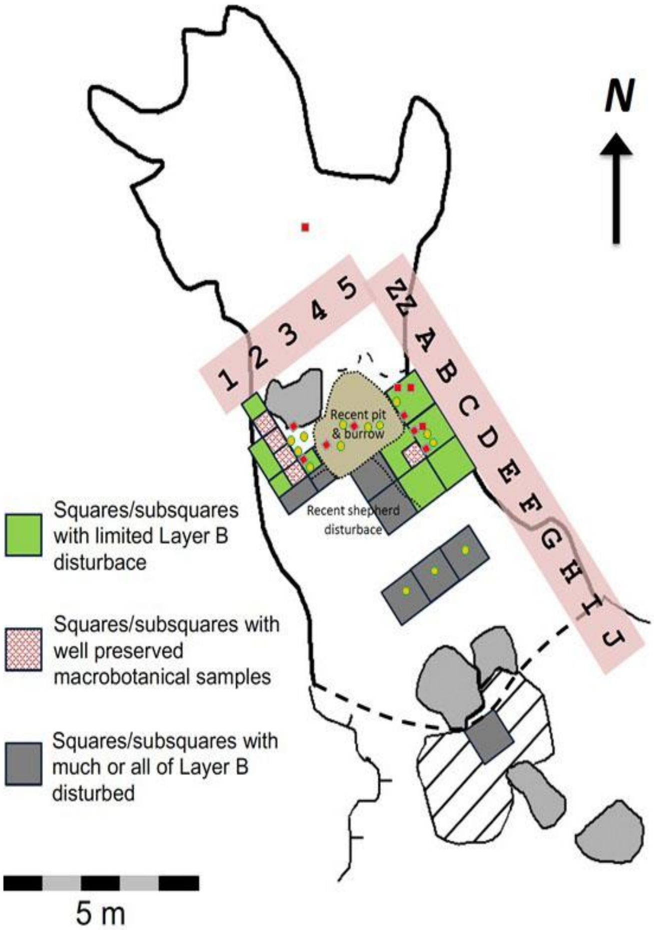

Fig. 4. Map of the cave with the provenience of block samples (red squares) for micromorphological analyses, and loose samples (yellow dots) for microarchaeological analyses. Detailed information regarding samples provenience (square, subsquare and layer) is given in Table 2 and 3.

2.3 Phytoliths and faecal spherulites

The 68 sediment samples analysed by FTIR were also analysed for phytoliths and faecal spherulites.

Phytolith extraction was carried out following the methodology of Katz et al. (2010). Between 20 and 50 mg of sediment were placed in a 0.5 ml Eppendorf tube and 50 µl of HCl 6N were added. After the reaction disappeared, 450 µl of sodium polytungstate solution (SPT) $[Na_6(H_2W_{12}O_{40})\cdot H_2O]$ with a density of 2.4 g/ml were added. The tube was vortexed and sonicated for 10 minutes and then centrifuged for five minutes at 5000 rpm. The supernatant was removed and transferred to another tube. 50 µl of the aliquot were placed on a microscope slide and covered with a 24x24 mm coverslip. Phytoliths present in 20 visual fields at 200x were counted for phytolith quantification. Morphological identification was based on our own modern reference collection (www.phytcore.org) as well as standard literature (Mulholland and Rapp, 1992; Piperno, 2006; Twiss, 1992). The nomenclature of the phytoliths followed, whenever possible, the International Code for Phytolith Nomenclature (ICPN 2.0, Neumann et al., 2019). Generally, a minimum number of 200 recognisable phytoliths is desirable to obtain a reliable phytolith morphological interpretation (Albert and Weiner, 2001). In those cases where the minimum number of 200 phytoliths was not reached, we included samples with >80 recognisable morphotypes. This follows the results obtained by Rodríguez-Cintas et al. (2020), where it was shown that samples with lower amounts of phytoliths (between 50-200) had similar distribution of the dominant morphotypes to samples with higher numbers from the same sampled context.

High concentrations of faecal spherulites are associated with the dung of certain ruminants (Shahack-Gross et al., 2011), and their occurrence in sediments is an excellent biomarker for the presence of livestock. For this reason, they were used to delimit the recent disturbance caused by the herders. The methods used follow Gur-Arieh et al. (2013). Between 30 and 40 mg of dried sediment is sieved through a 150 µm sieve, to remove particles >150 µm. After that, 500 µl of SPT with a density of 2.4 g/ml was added and the sample was sonicated for 10 minutes to disaggregate all the elements. 50 µl of the solution was placed on a microscope slide and covered with a 24x24 mm cover-slide. Microremains were identified under polarised light at 400x. Along with faecal spherulites, we also looked for ash pseudomorphs (major component of wood ash).

3. Results

3.1 Micromorphology

Micromorphology samples were grouped under four microfacies types (MFT) (Table 2): silty clay, silt, dispersed anthropogenic components, and bedded anthropogenic components. The latter two include a subtype characterised by extensive diagenesis, represented by total absence of bone. Descriptions and terminology follow Stoops (2021).

MFT name	Description	Process	Sample # (square/layer)
Silty clay	**c/f related distribution:** single-spaced to open porphyric (within aggregates). **Structure and voids:** crumb microstructure with compounds and complex packing voids; channel microstructure with channels. **Coarse fraction:** silt-sized, sub-angular quartz grains (dominant); medium sand-sized sub-rounded quartz grains (few); charcoal fragments (few); bone fragments (very few). **Fine fraction:** brown to reddish clay with speckled and grano-striated b-fabric. **Pedofeatures:** phosphate intergrowths; Fe-Mn nodules; silt infillings.	Colluvium, bioturbation, dissolution	9 (A2/Layer B)
Silt	**c/f related distribution:** monic (silt beds); double-spaced coarse enaulic (phosphate beds). **Structure and voids:** single-grain microstructure with simple packing voids (silt	Sheetwash, dissolution	3 (B2/Layer B)

	beds); intergrain microaggregate microstructure with complex packing voids (phosphate beds). **Coarse fraction:** fine silt-sized sub-angular quartz grains (very dominant). **Fine fraction:** phosphate crystals, no b-fabric. **Pedofeatures:** phosphate nodules.		
Dispersed anthropogenic components	**c/f related distribution:** single-spaced to open porphyric (within aggregates). **Structure and voids:** crumb microstructure with compound and complex packing voids; channel microstructure with channels. **Coarse fraction:** silt-sized, sub-angular quartz grains (dominant); medium sand-sized sub-rounded quartz grains (few); limestone pebbles (few); flint flakes (very few); bone fragments (frequent); charcoal fragments (few). **Fine fraction:** pale-brown to brown clay with faint or speckled b-fabric; dung spherulites. **Pedofeatures:** phosphate impregnations, intergrowths and nodules; calcium carbonate intergrowths and infillings; microfauna channels and burrows.	Combustion, bioturbation, dissolution	1 (B5), 2 (B5), 12 (C5) (all Layer B)
Dispersed anthropogenic components (no bone)	**c/f related distribution:** single-spaced to open porphyric (within aggregates). **Structure and voids:** crumb microstructure with compound and complex packing voids; channel microstructure with channels. **Coarse fraction:** silt-sized, sub-angular quartz grains (dominant); medium sand-sized sub-rounded quartz grains (few); limestone pebbles (few); flint flakes (very few); charcoal fragments (few); shell fragments (very few, samples 4 and 5). **Fine fraction:** pale-brown to brown clay with faint or speckled b-fabric; dung spherulites, crystallitic b-fabric (samples 4 and 5). **Pedofeatures:** extensive phosphate impregnations, intergrowths and nodules; microfauna channels and burrows.	Combustion, bioturbation, dissolution	3 (B2/Layer B), 4 (B2/Layer A), 5 (B2/Layer A), 14 (B3/Layer A), 15 (B3/Layer A) (note that samples 14 and 15 appeared in the field to consist of redeposited cemented blocks originating from Layer B)
Bedded anthropogenic components	**c/f related distribution:** single-spaced to open porphyric (within aggregates).	Combustion, dissolution	8 (B5), 11 (C5), 16 (C5) (all Layer B)

	Structure and voids: crumb microstructure with compound and complex packing voids; channel microstructure with channels and chambers. **Coarse fraction:** silt-sized, sub-angular quartz grains (dominant); medium sand-sized sub-rounded quartz grains (few); limestone pebbles (few); flint flakes (very few); bone fragments (frequent); charcoal fragments (few); phytoliths (very few). **Fine fraction:** pale-brown to reddish clay with faint or speckled b-fabric. **Pedofeatures:** phosphate intergrowths and nodules.		
Bedded anthropogenic components (no bone)	**c/f related distribution:** single-spaced to open porphyric (within aggregates). **Structure and voids:** crumb microstructure with compound and complex packing voids; channel microstructure with channels and chambers. **Coarse fraction:** silt-sized, sub-angular quartz grains (dominant); medium sand-sized sub-rounded quartz grains (few); limestone pebbles (few); flint flakes (very few); charcoal fragments (few); phytoliths (very few). **Fine fraction:** pale-brown to reddish clay with faint or speckled b-fabric. **Pedofeatures:** extensive phosphate intergrowths and nodules.	Combustion, dissolution	6 (A2), 7 (A2) (Layer B)

Table 2. Micromorphological descriptions of the MFTs. The terminology follows Stoops (2021).

3.1.1 Silty clay

Sample 9 from square A2 (western area) (Fig. 4) is composed mainly of small aggregates of silty clay, characterised by overall high porosity although in places they show evidence of compaction (without bedding). Clay minerals are brown to reddish in colour and exhibit speckled birefringence fabric (b-fabric), and grano-striated b-fabric around quartz grains. Anthropogenic materials include charcoal fragments, which occur in small numbers throughout the sample, and very few fragments of bone. Calcium carbonate is absent, whereas pedofeatures include phosphate nodules and iron-manganese nodules (Fig. 5a and 5b). Rare silt infillings are also present.

3.1.2 Silt

In square B2 (western area) (Fig. 4), part of sample 3 exhibits alternating beds of pure quartz silt and phosphate nodules (Fig. 5c and 5d). The latter are grey in plane polarised light and isotropic in cross polarised light and appear substantially different from calcium phosphate nodules observed ubiquitously in all other contexts. No anthropogenic components were observed.

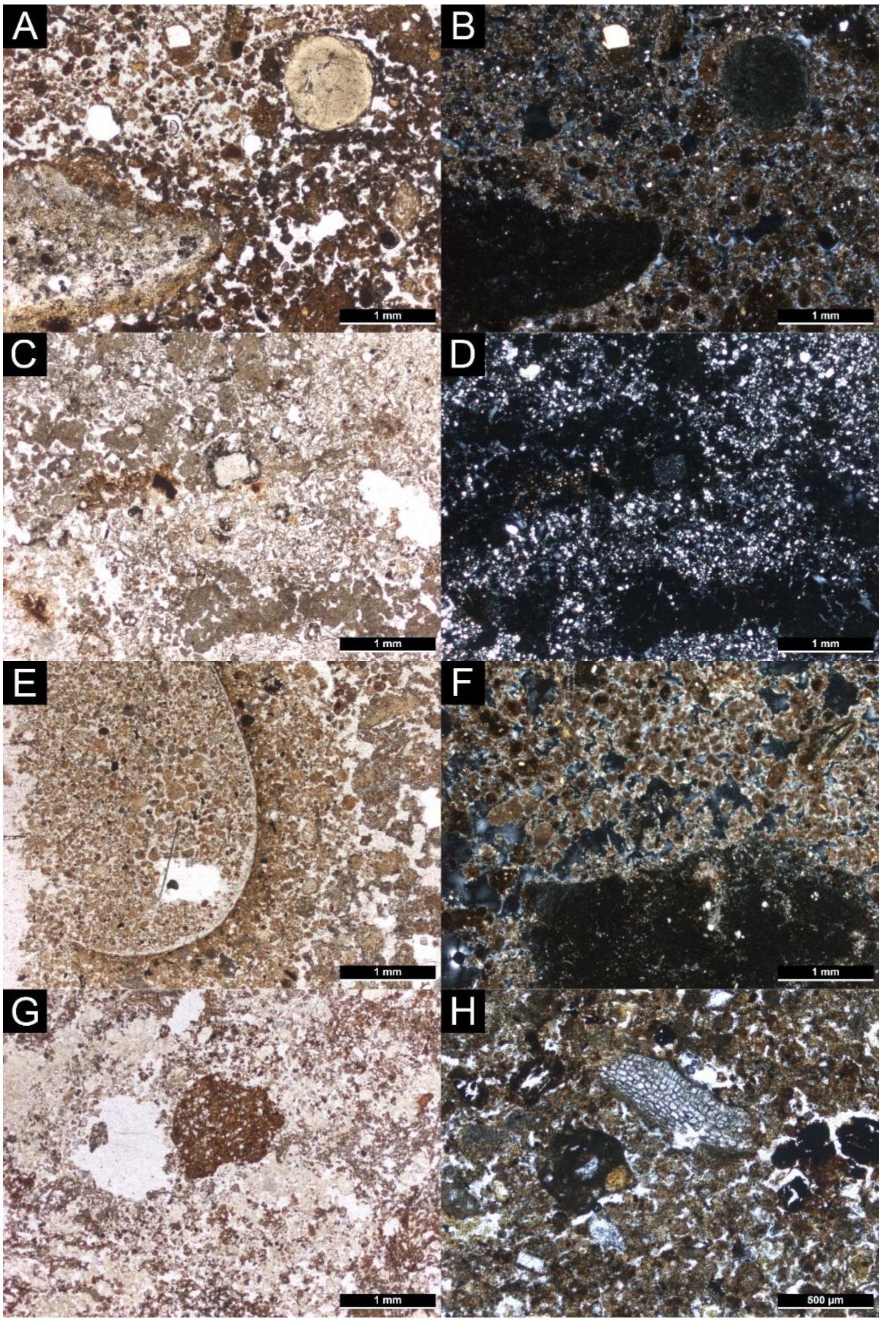

Fig. 5. Photomicrographs of micromorphology thin sections. A-B: authigenic phosphate nodules; note their isotropic nature in cross-polarised light (B); C-D: alternating beds of authigenic phosphate nodules and silt, the latter exhibits bright interference colour in cross-polarised light (D); E: burrow filled with clay aggregates; F: aggregates of recrystallised ash in cross-polarised light; G: rounded pellet of red silty clay embedded in a matrix rich in secondary phosphates; H: ashed plant fibre (now phosphatised calcium carbonate) retaining the original cellular structure.

3.1.3 Dispersed anthropogenic components

Most contexts are grouped under this MFT. Aggregates of silty clay, including large fragments of bone (some of which are burnt) and charcoal, are characterised by high porosity and little compaction and are dispersed throughout the sample, with clear evidence of bioturbation (Fig.

5e). Burrows and channels produced by microfauna are common in all samples and in places contain calcitic dung spherulites, including in the groundmass in samples 4 and 5 (square B2) (Fig. 4). Furthermore, samples 4 and 5 are rich in shells of land snails, which appear to be well preserved based on their interference colour. Aggregates of recrystallised and phosphatised calcium carbonate ash and/or secondary calcium carbonate infillings are common in a few samples (Fig. 5f). Large (cm-sized) aggregates and smaller rounded pellets of reddened silty clay are common in all samples, and exhibit different types of b-fabric, from faint to speckled (Fig. 5g). Very few flint artefacts occur as well. More than half of the samples are assigned to a subtype of the MFT where no bone or calcium carbonate is preserved (except for land snail shells in samples 4 and 5) and phosphate intergrowths and nodules occur throughout the thin section.

3.1.4 Bedded anthropogenic components.

Five samples exhibit beds of phosphatised ash and/or red clay. There is a marked distinction between contexts where bone is not preserved (MFT subtype characterised by extensive diagenesis), rich in authigenic phosphate nodules and intergrowths of different mineralogy, and contexts where bone is well preserved, together with phosphatised calcium carbonate ash, limestone pebbles with reaction rims, and secondary calcium carbonate. Two samples exhibit ashed and phosphatised calcium carbonate plant fibres (phosphatised calcium carbonate) that retain the original cellular structure (Fig. 4H). Phytoliths occur in one context but are not clearly visible due to stacking with phosphates. Red clay pellets are common, and in sample 16 red clayey sediment occupies the entire lower portion of the thin section (Fig. 5). Post-depositional processes include the dissolution of bone minerals and extensive precipitation of authigenic phosphates, and bioturbation from microfauna.

Fig. 6. Scan of a representative thin section of the MFT characterised by bedded anthropogenic components (sample MHM10 16a, square C5), showing loose charcoal, bone fragments, and red clay pellets resting on top of a compact, reddened substrate (dashed line).

3.2 FTIR

Three mineralogical groups were identified through FTIR-analysis: silicates, carbonates, and phosphates (Fig. 7).

3.2.1 Silicates

Terra rossa clay is the largest silicate component and forms the sediment matrix (Table 3). Terra rossa is a silty to clayey reddish soil, composed of clay, quartz, calcite, and oxides, and is widespread through the Mediterranean area (Durn et al., 2014). Clay minerals identified in Layer B (squares A1 and A2) have a diagenetically altered structure (Table 3). Additionally, clay minerals showing thermal alteration are observed in samples from square C5 (eastern area), squares F2-4 (front sounding), square B2a (western area), and square B3 (central area) (Fig. 4, Table 3). Quartz is also present in all contexts (Fig. 7, Table 3).

Siliceous aggregates are present in almost all samples (Table 3). They are an important component of wood ash and consist of fine-grained crystalline minerals embedded into a biogenic silica matrix.

3.2.2 Carbonates

Calcite was documented in eight samples, mainly in squares F2, F3, and F4 (front sounding Layers A and B), but also in square B2a (western area, Layer B), and C9 (eastern area) (Fig. 7, Table 3). In all cases, calcite derived from wood ash. Two samples are associated with the MFT 'dispersed anthropogenic components' (sample B1 from mixed Layer B material redeposited in Layer A fill; and the superficial sample C9) (Fig. 7, Table 3).

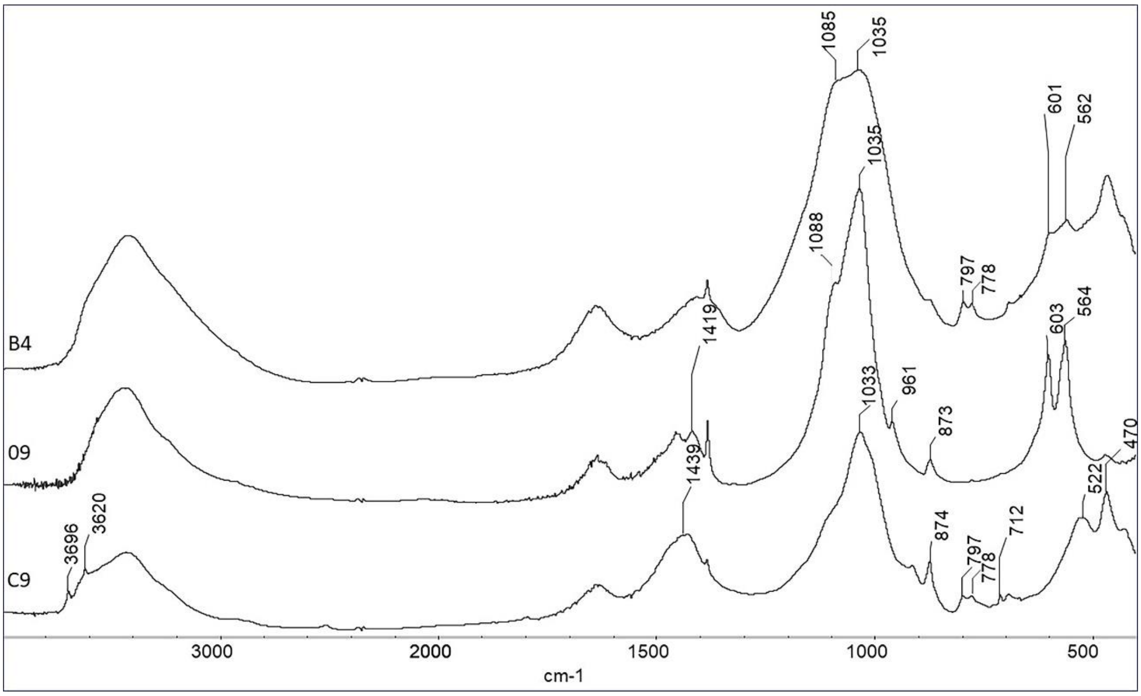

Fig. 7. FTIR from different samples from MHM showing their main components: C9) unburnt clay (3696, 3620, 1033, 522, 470 cm^{-1}); geogenic calcite (1439, 874, 712 cm^{-1}); 09) carbonate hydroxylapatite (1419, 1035, 603, 564 cm^{-1}); B4) burnt clay (1035, 797, 778 cm^{-1}); apatite (601, 562 cm^{-1}).

3.2.3 Phosphates

Authigenic phosphate minerals, such as carbonate hydroxylapatite, resulting from the interaction between phosphorous derived from the decay of organic material and calcite (Shahack-Gross et al., 2005), were identified in some samples where shepherds' disturbance was indicated by the identification of faecal spherulites. Yet, carbonate hydroxylapatite was detected in samples from the eastern area of the cave (square C5) and it is noteworthy that these samples do not show spherulites. Additionally, sample 9, collected from the bedrock exposed in square A2, is composed of pure carbonated hydroxylapatite (Fig. 7, Table 3). Variscite and montgomeryite were observed in two samples from the western area (squares A1 and A2) (Fig. 4, Table 3). These minerals result from the dissolution and recrystallisation of more soluble components (carbonates) as the pH of the sediments decreases (Weiner et al., 2002). Transforming apatite was noted in the eastern area of Layer B, squares B4 and B5 (Table 3). Apatite is the most ubiquitous phosphate mineral in soils and can be composed of different mineral phases (apatite transforming) resulting from continuous dissolution and recrystallisation processes (Karkanas et al., 2002). Finally, amorphous calcium iron phosphate, probably an authigenic mineral that incorporates different elements, was detected in Layer B, squares A1, A2 and B1 (Table 3).

3.3 Faecal spherulites

Spherulites (Fig. 8 a) were documented in 20 samples (six from Layer A, 13 from Layer B, and in one that could not be assigned either to Layer A or B (F5 and F2) (Fig. 4, Table 3). Sample B9 (square B4) is the only sample from Layer A where spherulites were not observed. In Layer B, they were observed in squares F3, F4, B2, A2 (western area), and B5 (Fig. 4, Table 3). Conversely, no ash pseudomorphs were observed in the samples.

Lab #	Square	Subsquare	Layer	Phytoliths per g. of sediment	#Phytolith identified	Spherulites per g. of sediment	Weathering (%)	FTIR
F1	F2	A-B	A	1,000,000	322	7,100,00	10.8	Cl(b), Ca(a), SA, Qz
F2	F3	C-D	B	408,000	184	887,000	4.2	Cl(b), Ca(a) CHA, Qz SA,
F3	F3	C-D	B	260,000	176	811,000	7.9	Cl(b), Ca(a), CHA, SA, Qz
F4	F4	C	A	770,000	262	1,000,000	5.1	Cl(b), Ca(a), SA, CHA, Qz
F5	F2	A-C	?	173,000	167	20,000	1.8	Cl(b), Ca(a), CHA, Qz SA
F6	F2	C-D	A	167,000	248	1,900,000	3.9	Cl(b), Si, Ca(a), Qz
F7	F2	C-D	?	95,000	241	0	5.9	Cl, Sanidine
F8	F4		B	104,000	204	959,000	4.7	Cl (b), SA, CHA, Qz
B1	B2	A	B	534,000	248	466,000	3.9	Cl (b), Ca(a), SA, CHA
B2	B2	A	B	13,500	22	0	18.5	Cl, SA, Qz
B3	B2	A	B	13,000	65	14,000	0.0	Cl, SA,
B4	B2	A	B	196,000	199	0	6.1	Cl(b), Ap(t) SA, Qz
B5	B2	A	B	123,000	229	0	24.2	Cl(b), Ap(t), SA, Qz, ACIP
B6	B3	B	B	113,000	65	44,000	3.0	Cl(b), SA, Qz, ACIP
B7	B3	B	A	377,000	224	830,000	4.7	Cl(b), SA, Qz, CHA
B8	B4	A	A	245,000	231	18,000	4.9	Cl, CHA, SA
B9	B4	A	A	95,000	205	0	3.3	Cl, SA, Qz, CHA

B10	B4	A	A	252,000	199	1,300,000	12.3	Cl, CHA, SA
C1	C5	A	B	2,000	31	0	72.8	Cl(b) SA, CHA
C2	C5		B	145,000	185	0	15.1	Cl (b), SA, CHA
C3	C5	C	B	53,000	147	0	21.8	Cl, SA, Qz, CHA?
C4	C5	A-C	B	22,000	85	0	19.1	Cl, SA, Qz, CHA?
C5	C5	C	B	6,000	7	0	22.2	Cl(b), SA, Lp
C6	C5	A	B	2,000	24	0	11.1	Cl(b), CHA, SA
C7	C5	C	B	1,000	7	0	46.2	Cl(b), CHA, SA?
C8	C5	A	B	3,000	9	0	35.7	Cl, CHA, SA, Qz
C9	C5	surface	surface	86,000	81	0	2.4	Cl, Ca, Qz,
1	A1	D	B	13,000	8	0	27.3	Cl(t), Ap(t), ACIP
2	A1	D	B	0	0	0	0.0	Cl(t), Qz, SA
3	A1	D	B	0	0	0	0.0	Cl(t), Qz, CHA, SA
4	A1	D	B	0	0	0	0.0	Cl(t), Qz, SA
5	A1	D	B	69,000	5	0	37.5	Cl(t), Qz, SA
6	A1	D	B	0	0	0	0.0	Cl(t), Qz
7	A1	D	B	0	0	0	0.0	Cl(t), ACIP, Qz
8	A1	D	B	0	0	0	0.0	Cl(t), ACIP,Qz
25B	A1	D	B	0	0	0	0.0	Cl(t), Mo(t), SA
26	A1	D	B	0	0	0	0.0	Cl(t), SA, ACIP
27	A1	D	B	0	0	0	0.0	Cl(t), SA, ACIP
28	A1	D	B	0	0	0	0.0	Cl(t), SA, ACIP
29	A1	D	B	15,000	100	0	20.3	Cl(t), Qz
30	A1	D	B	0	0	0	0.0	Va, SA
31	A1	D	B	0	0	0	0.0	Va, SA
50	A1	B	B	0	0	0	0.0	Cl(t), ACIP, SA
51	A1	B	B	36,000	102	0	13.9	Cl(t), ACIP, SA
52	A1	B	B	0	0	0	10.8	Cl(t), ACIP, SA
9	A2	C	B	0	0	0	0.0	CHA
10	A2	C	B	0	0	0	0.0	Cl(t), ACIP, SA, Qz
11	A2	C	B	0	0	0	0.0	Cl(t), CHA(t), ACIP
12	A2	C	B	0	0	0	0.0	Cl(t), Qz, ACIP
13	A2	C	B	0	0	0	0.0	Cl(t), Qz, ACIP, SA
14	A2	C	B	0	0	0	0.0	Cl(t), Qz, ACIP
15	A2	C	B	24,000	4	0	0.0	Cl(t), Qz, ACIP
16	A2	C	B	7,000	7	0	30.0	Cl(t), Qz, ACIP

17	A2	C	B	0	0	0	0.0	Cl(t), Qz, ACIP, SA
18	A2	C	B	0	0	0	0.0	Cl(t), ACIP, Ap(t), SA
19	A2	C	B	212,000	192	374,000	0.0	Cl(t), SA, Qz, ACIP
20	A2	C	B	23,000	5	0	0.0	Cl(t), SA, ACIP, Mo
21	A2	C	B	0	0	0	0.0	Cl(t), Qz, SA, ACIP
22	A2	C	B	34,000	15	0	0.0	Cl(t), SA, ACIP, Mo(t)
38	B4	B	B	1,101,000	196	1,750,000	9.7	Cl, Ap(t), SA
40	B4	B	B	211,000	123	85,000	3.1	Ap(t), Cl(t), SA
32	B5	B	B	25,000	14	30,000	0.0	Cl, Ap(t), SA
33	B5	B	B	79,000	36	89,000	0.0	Cl, Ap(t), SA
34	B5	B	B	0	0	0	0.0	Cl, Ap(t), SA
35	B5	B	B	45,000	100	0	5.7	Cl, Ap(t), SA
36	B5	B	B	203,000	50	1,140,000	3.8	Cl, Ap(t), SA
37	B5	B	B	311,000	101	394,000	4.7	Cl(t), Ap(t), SA
39	B5	A	B	41,000	8	0	0.0	Cl, Ap(t), SA

Table 3. List of the 68 samples analysed and their provenience, as well as the results: estimated number of phytoliths per gram of material, number of phytoliths morphologically identified, percentage of weathered phytoliths (chemical alteration), estimated number of faecal spherulites per gram of material, and FTIR results. Ca: Calcite; Cl: clay; SA: siliceous aggregates; CHA: carbonate hydroxylapatite; Si: silica; Qz: quartz; ACIP: amorphous calcium iron phosphate; Ap: apatite; Mo: montgomeryite; Va: variscite; (a): ash derived; (b) burnt; (t): transforming

3.4 Phytoliths

Phytoliths were identified in both Layers A and B. Samples from Layer A show concentrations of phytoliths per gram of sediment between 86,000 (C9) and 1,000,000 (F1) (Table 3) and are associated with the presence of spherulites, except for sample B9 from the eastern area (square B4), which yielded a lower concentration of phytoliths and no spherulites (Table 3). Phytolith concentrations in Layer B ranged from 7,000 (16, square A2) to 196,000 (B4, square B2) (Table 3). The percentage of weathered phytoliths varies between 5.7% and 24.2% (Table 3). PCA analysis was performed in samples with >80 morphotypes identified, and the distribution of morphotypes shows that samples from Layer A cluster together (with the exception of sample F1), with a higher proportion of grasses, while samples from Layer B have higher proportions of dicot morphotypes (Fig. 9).

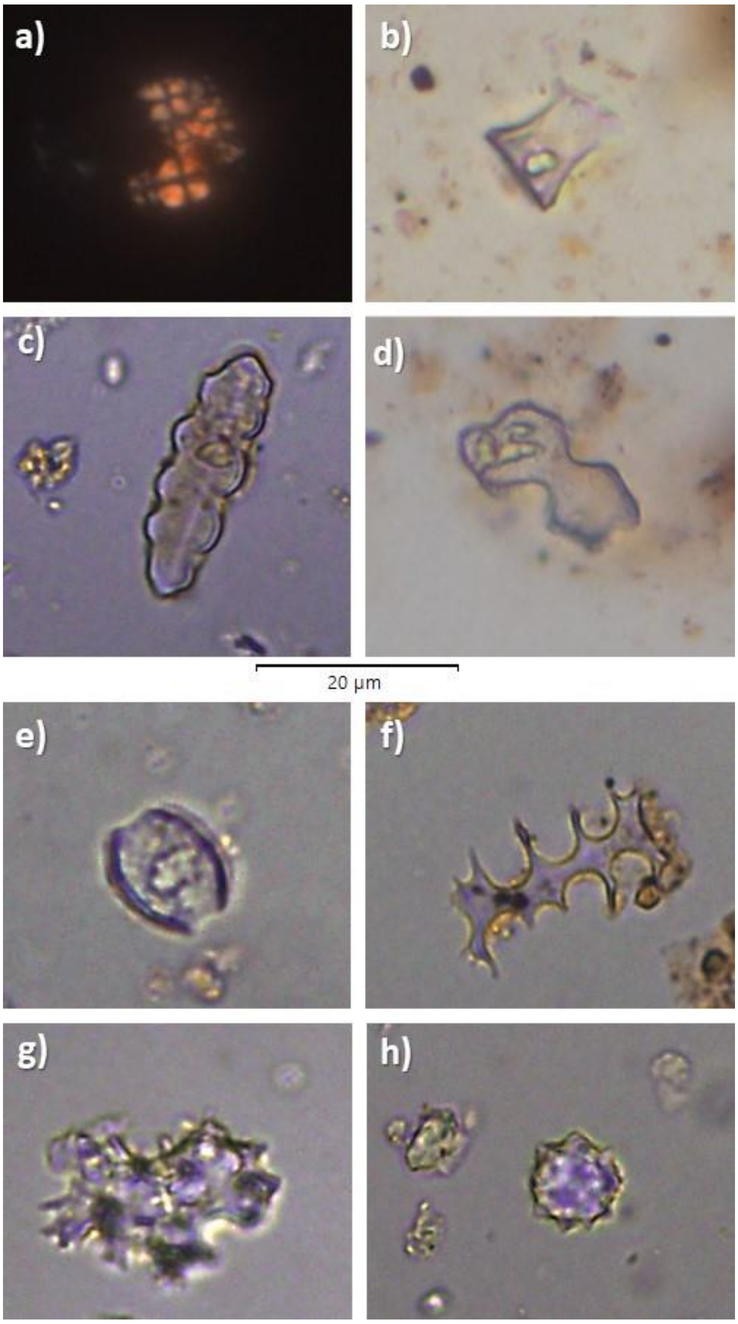

Fig. 8. Microphotographs of faecal spherulites and phytoliths. Images taken at 400x: a) faecal spherulites from sample B7; b) GSSCP Rondel pyramidal with a keeled top from sample 19; c) Crenate from sample B4; d) GSSCP Bilobate with the lobes ends convex, from sample 33; e) Saddle from sample 29; f) Elongate dendritic from sample C3; g) Irregular verrucate characteristic of dicots fruits from sample B4; h) Spheroid echinate characteristic palm phytolith from samples 51.

Layer A shows a high number of faecal spherulites and therefore these levels were interpreted as highly disturbed and were not included in our phytolith study of the EUP layers. On the contrary, most samples from layer B did not show the presence of spherulites and were interpreted as not having been disturbed by intrusive microbotanical traces. Therefore, our study focused on those Layer B-associated samples where faecal spherulites were absent. In these spherulite-free Layer B samples, 24 different morphotypes were identified (Table 4. Phytoliths morphologically identified in undisturbed samples from Layer B, botanical attribution, and average presence in the samples.

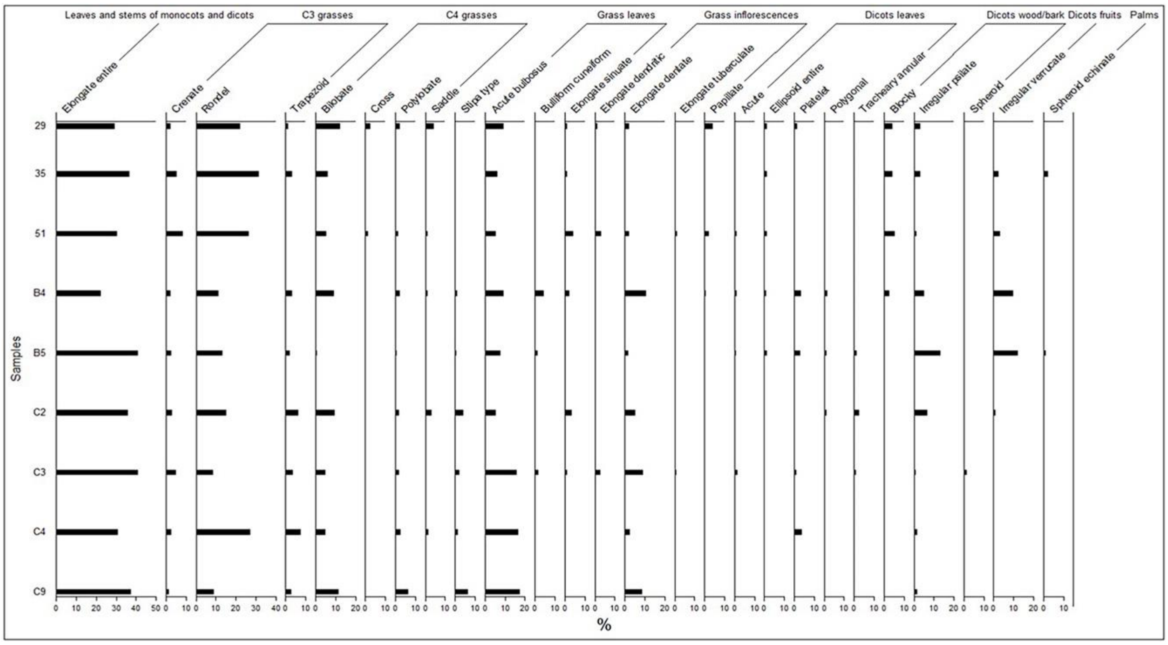

Fig. 10. Plot with then relative abundance of each morphotype identified in the undisturbed samples from Layer B, grouped accordingly to their attributions.

). Whenever possible, morphotypes were grouped into different categories based on their taxonomic and anatomical provenance: Poaceae (C_3 and C_4), Poaceae leaves/stems, Poaceae inflorescence, dicots wood/bark, dicot leaves, dicot fruits, and palms. ELONGATE ENTIRE was not included in these groups because, although this morphotype is commonly produced in the stems of grasses and sedges, it can also be found in dicotyledonous plants in lesser numbers (ICPN 2.0, Neumann et al., 2019) (Fig. 11). The relative abundance of each morphotype identified can be found in the supplementary material.

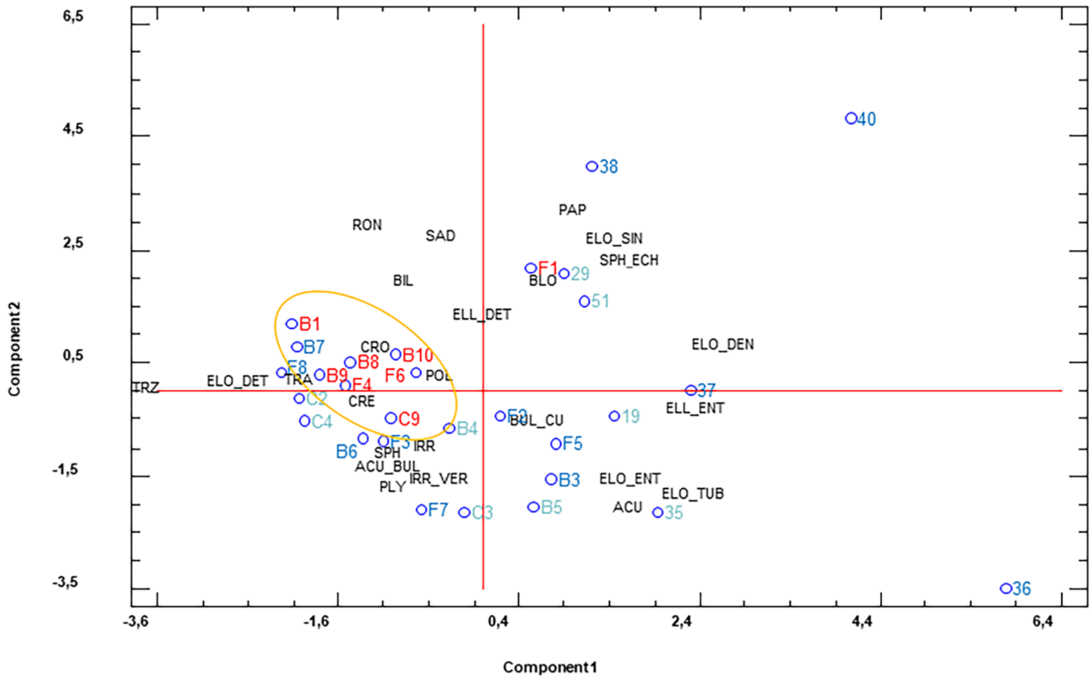

Fig. 9. PCA run over morphotypes and samples from Layers A and B (n=29). Sample provenance is indicated by colours: red: Layer A; blue: disturbed (presence of spherulites) Layer B; and green undisturbed (absence of spherulites) Layer B.

Morphotype	Botanical attribution	Average %
Elongate entire	Leaves and stems of monocots and dicots	33.6
Rondel	C_3 grasses	18.1
Acute bulbosus	Grass leaves	10.1
Bilobate	C_4 grasses	6.9
Elongate dentate	Grass inflorescences	5.1
Irregular psilate	Dicots wood/bark	3.8
Irregular verrucate	Dicots Fruits	3.4
Crenate	C_3 grass leaves	3.3
Blocky	Dicots wood/bark	3.1
Trapezoid	C_3 grasses	3.1
Polylobate	C_4 grasses	2.1
Bilobate trapezoid	Stipeae tribe	2.0
Cross	C_4 grasses	1.5
Platelet	Dicots leaves	1.4
Elongate sinuate	Grass leaves	1.3

Saddle	C_4 grasses	1.2
Bulliform cuneiform	Grass leaves	0.9
Ellipsoid entire	Dicots leaves	0.9
Elongate dendritic	Grass inflorescences	0.8
Papillate	Grass inflorescences	0.8
Spheroid echinate	Palms	0.7
Acute	Dicots leaves	0.5
Tracheary annular	Dicots leaves	0.5
Polygonal	Dicots leaves	0.5
Spheroid	Dicots wood/bark	0.3
Elongate tuberculate	Grass inflorescences	0.2

Table 4. Phytoliths morphologically identified in undisturbed samples from Layer B, botanical attribution, and average presence in the samples.

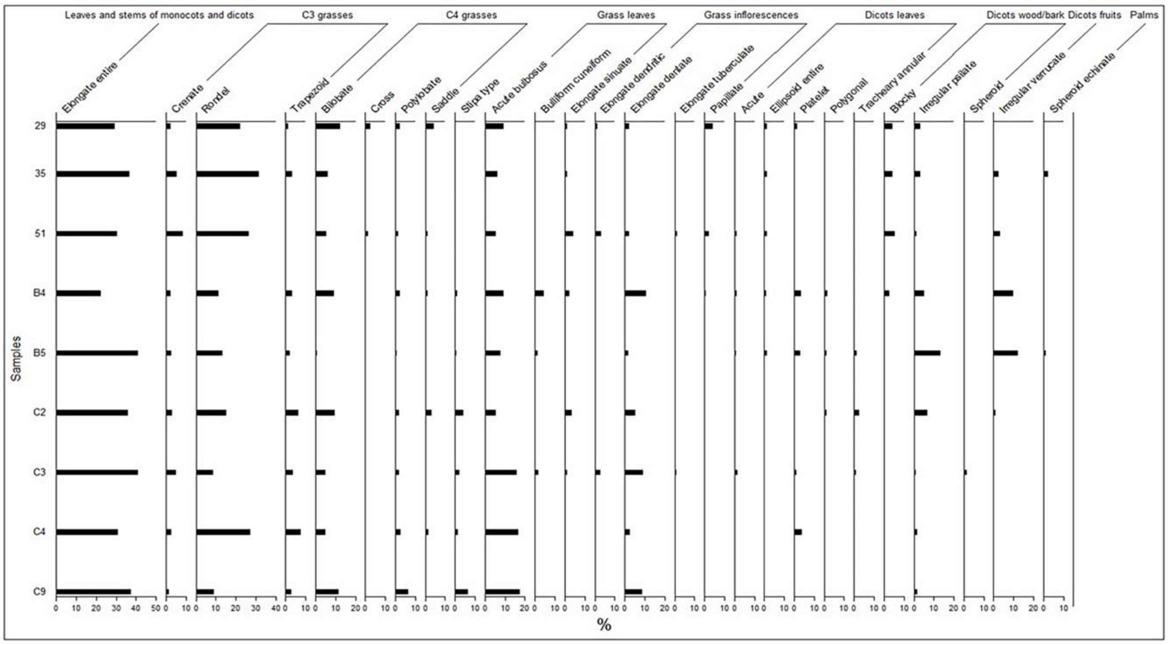

Fig. 10. Plot with then relative abundance of each morphotype identified in the undisturbed samples from Layer B, grouped accordingly to their attributions.

The most abundant morphotypes noted were the Grass Silica Short Cell Phytolith (GSSCP) from the Poaceae family, particularly Rondel (18.1%), and Trapezoid (3.1%) (Table 4, Fig. 8 b, c, Fig. 10 and Fig. 11). Also, Crenate morphotype was documented (3.3%). These morphotypes are most identified in C_3 grasses such as pooids, for example *Poa bulbosa* and *Dactylis glomerata*, abundant in the area (Taifour and El-Oqlah, 2016). Other GSSCP identified were Bilobate (6.9%) (Fig. 8 d), Polylobate (2.1%) and Saddle (1.2%) (Table 4, Fig. 8 e and Fig. 10). Bilobate are found in the C_4 Panicoideae subfamily and in certain C_3 plants such as Stipeae tribe and Arundinoideae subfamily (Chauhan et al., 2011; Shakoor et al., 2014). The Bilobate identified, with narrow lobes and trapezoidal section, has the typical characteristics produced by the Stipeae tribe (Blinnikov, 2005; Fredlund and Tieszen, 1994) (Table 4, Fig. 10). Square C5 (eastern area) had a higher concentration of these morphotypes (>6%). SADDLES are widely produced by C_4 plants of the Chloridoideae and Bambusoideae subfamilies, and are associated with drier environments (Bremond et al., 2008; Fredlund and Tieszen, 1994). Phytoliths characteristic of the inflorescence of grasses were also identified (<12.2%) (Table 4, Fig. 11). This plant part is represented by ELONGATE with decorate margins: E. DENTATE (5.1%), E. DENDRITIC (0.8%) (Fig. 8 f) and E. TUBERCULATE (0.2%) and by PAPILLATE (Table 4).

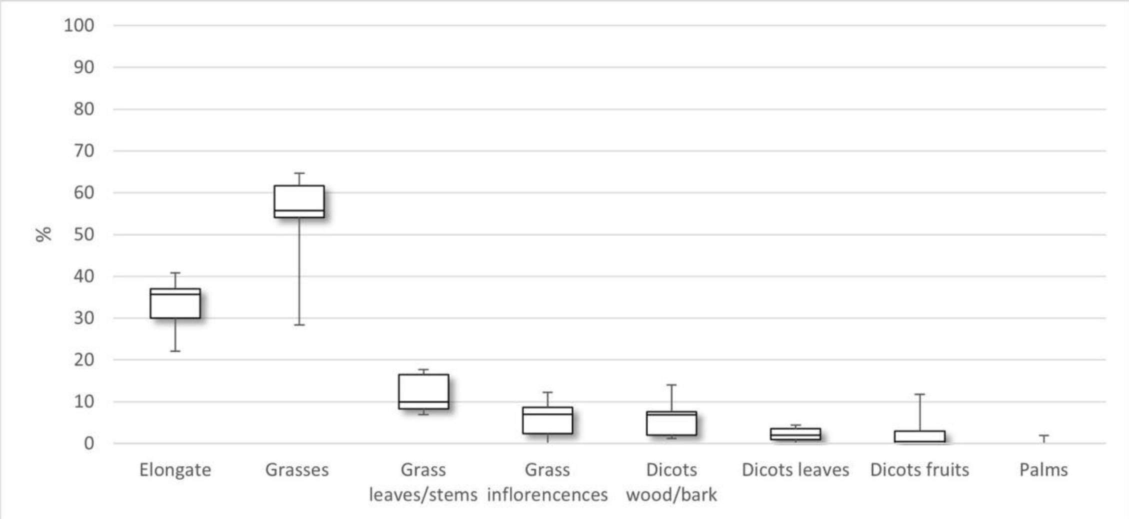

Fig. 11. BoxPlot showing the percentage presence of the different phytoliths identified in undisturbed Layer B samples (n=9), grouped by their taxonomic and anatomical provenience in plants. Elongates have been kept separated as per their low taxonomic value. The mean values (mid-line), standard error ± (box) and standard deviation (whiskers) are given for the plant types and plant part.

Dicot phytoliths were present in samples from the western area, including sample 29 (square A1), samples B4 and B5 (square B2) and from the eastern area, sample 35 (square B5) with percentages ranging from 9% to 18% (Fig. 10). Within the dicots, morphotypes from wood and bark were more abundant (IRREGULAR PSILATE (3.8%) and BLOCKY (3.1%)) than those from leaves (PLATELET (1.4%), ELLIPSOID (0.9%), TRACHEARY ANNULAR (0.5%), POLYGONAL (0.5%) and SPHEROID (0.3%)). IRREGULAR VERRUCATE (Fig. 8 g), common in dicot fruits (Runge 1999), occurred mainly in samples B4 and B5 from square B2 (11.8%) (Fig. 10 and Fig. 11). Finally, SPHEROID ECHINATE (Fig. 8 h), which is widely produced in palms (Albert et al., 2009) are also present in samples 51 (square A1) and B5 (square B2), although at a low percentage (<2%) (Fig. 10 and Fig. 11).

4. Discussion

4.1 Sedimentary context

The mineralogical composition of the samples analysed in this study reflects the terra rossa sedimentary context of the site. This is supported by the occurrence of clay minerals in the FTIR spectra. The identification of authigenic phosphates, confirms the presence of components originated from the degradation of organic matter. Additionally, wood ashes are also part of the sediments as revealed by the presence of siliceous aggregates and pyrogenic calcite in the FTIR.

The crumb microstructure exhibiting different degrees of compaction and the grano-striated b-fabric of the silty clay sediment (sample 9, Layer B) can be associated to a certain degree of colluvial transport, possibly involving human agency in the case of dispersed anthropogenic components including charcoal, burnt bone, and red silty clay pellets (Layer B samples 1-3 and 12 and Layer A/redeposited Layer B samples 4-5 and 14-15) (Goldberg et al., 2009). The bedded anthropogenic material, on the contrary, is the result of primary deposition by the EUP occupants (Layer B samples 6-8, 11, 16). In the case of the silt MFT (observed in Layer B sample 3, square B2), the absence of fine fraction in the silt beds indicates that they were deposited by low-energy water, as in sheetwash (Toffolo et al., 2017). Given that this sedimentary structure occurs in only one in situ sample from Layer B, it is not possible to verify whether the depositional process is localised, or it affected the entire cave.

4.2 Preservation

The results confirm the uneven preservation of the MHM EUP-associated Layer B deposit. Two distinct areas can be identified.

4.2.1 Western area

Archaeological observations in the field noted the absence of bone, combined with macroscopic white and yellow nodules suspected to be phosphate concretions. This suggested post-depositional bone dissolution within square B2 (Stutz et al., 2015). The dissolution can be explained by the presence of the low-energy water sources identified by micromorphology in sample 3. In squares A1 and A2 both micromorphological and FTIR results highlight the presence of phosphate minerals formed in low pH sediments, where bones tend to dissolve (pH <7.2) (Weiner et al., 1993). This also explains the absence of calcium carbonate, the main component of ash and the mineral from which these more insoluble minerals recrystallise (Karkanas et al., 2002). Regarding the silty clay MFT (square A2), the rare silt infillings observed reflect coarse water movement down the profile, whereas the iron-manganese nodules are caused by the oxidation of ions mobilised by the decay of organic material (Vepraskas et al., 2018).

More generally, cycles of wetting and drying favoured the nucleation of phosphate nodules, which is related to the evaporation of water saturated in phosphate ions originating from the dissolution of organic matter and/or bones (Karkanas et al., 2000; Shahack-Gross et al., 2004). The intensity of post-depositional processes varies considerably within the western area. It includes extreme results where no bone is preserved, and only extensive authigenic phosphate intergrowths and nodules of variable mineralogy remain. The better-preserved samples show aggregates of recrystallised calcium and phosphatised carbonate ash, as well as recent land snail shells made of calcium carbonate. This high variability in the effects of diagenetic alteration of the sediments is common in limestone and dolomite caves in the southern Levant, as shown at sites such as Kebara, Hayonim, and Manot, located west of the Jordan Valley (Albert et al., 2012; Berna et al., 2021; Mercier et al., 1995; Schiegl et al., 1996; Weiner et al., 2007; Weiner et al., 1993; Weiner et al., 2002). Conversely, abundant, and well-preserved wood charcoal (i.e., *Quercus* deciduous type, *Pistacia*, *Amygdalus*), charred seeds (i.e., large-seeded legumes, *Pistacia, Ficus*) (White et al., 2019) and fruit and dicotyledonous phytoliths are well represented in the western area. Therefore, our results suggest that post-depositional processes in the western area would have affected the preservation of bones, but not the macro- and microbotanical remains.

4.2.2 Eastern area

Interestingly, all the micromorphological samples from the eastern side of the cave (row 5 of the site grid, Fig. 4) are clearly associated stratigraphically with Layer B, and they show bone and (to a smaller extent) calcium carbonate preservation, whereas Layer B samples from the western side are affected by bone dissolution and extensive phosphate growth. The Layer B samples from square C5 show the presence of combustion features, mineralogically composed of phosphates, particularly carbonate hydroxylapatite. Despite the presence of phosphates, bones are well preserved in this area, which is consistent with Weiner et al. (1993), who show that bones can be preserved in carbonated apatite contexts. Preliminary archaeobotanical results from this area suggest that legume seeds and nutshells may be less abundant than in the western area. Dicots fruit phytoliths are also less abundant in the eastern area, suggesting that fruit and other plant foods were mainly processed in the western area. Micromorphological samples 8 (square B5), 11, and 16 (C5), where bioturbation and diagenesis are low and there is clear distinction between combustion products and substrate, can be interpreted as hearths. In sample 16, the lower part of the thin section represents the intact substrate or reddened clay on which combustion occurred, as indicated by the overlying bed rich in phosphate ash, charcoal and burnt bone (Aldeias et al., 2016). The homogeneous mixture of bone, charcoal, and phosphates on this surface, which shows no evidence of bedding or horizontal fabric of the coarse components, may be interpreted as evidence of sweeping or trampling of combustion debris (Goldberg et al., 2009).

4.2.3 Variable effects of recent disturbance

Different post-depositional processes affected the contexts, based on the occurrence of pedofeatures. Almost all the micromorphological samples, except for 6, 7 (square A2), 8 (B5), and 16 (C5), are affected by bioturbation by microfauna, as evidenced by channels filled with churned up aggregates of silty clay. At least a small part of this activity was recent, based on the presence of calcitic dung spherulites in some samples, especially near the contact with Layer A, indicating disturbance by shepherd activities. Similarly, the fragments of land snail shells in Layer A-associated samples 4 and 5 (square B2) appear to be the result of recent faunal activity. These shells may represent the most recent episode of bioturbation, given the presence of authigenic phosphates, which are likely to have formed under conditions in which the calcium carbonate shells would have dissolved (Weiner, 2010).

The results confirm the archaeological observations suggesting that modern disturbance by shepherds occurred mainly in the central area of the cave (in square B3, and the boundary samples from squares A2, B2, B4 and B5) and in the sounding squares (F2, F3 and F4) affecting Layers A and B. This disturbance is well-defined, confirming that neither the western nor the eastern areas of the cave have been recently reworked. Therefore, the archaeological record (micro and macro) recovered from this central area (mainly square B3) does not represent an *in situ* EUP assemblage. The occurrence of transforming apatite at the boundary between samples of square B4 and B5 indicates continuous postdepositional alteration, if not strong diagenesis of the original ash, as suggested by the absence of leucophosphite (Weiner et al., 2002).

4.3 Plants present at the site

The phytolith record in Layer B samples from MHM shows an overall low concentration of phytoliths, which can have three possible explanations: i) dissolution, ii) the presence of non-rich phytolith-producing plants and iii) the absence of plants. We discard the third possibility, as charred seeds and charred wood remains have been widely identified in most of the samples (White et al., 2019). Regarding phytolith dissolution, the phytolith record shows little weathering. Phytoliths are well preserved at pH <8.2 (Cabanes et al., 2011), which seems to be the case for the sedimentary context at MHM. Therefore, the overall low concentrations of phytoliths must be explained by the diversity of plants present at the site, which are not phytolith-rich producer plants. Dicots make up a significant proportion of the undisturbed Layer B phytolith assemblage, including dicot fruit phytoliths. Both wood/bark, and dicot fruits produce low amounts of phytoliths and, as a result, are usually underrepresented in the phytolith record, particularly when compared to monocot plants (Albert & Weiner, 2001; Tsartsidou et al., 2007). Poaceae phytoliths are the most abundant in the assemblage (mean 50.4%) (Fig. 11). The question is whether their presence is due to their use as tinder or as contamination, as several studies show that they can be introduced as contamination by adhering to the wood/bark of the dicots, between 30 and 49% in the Mediterranean area (Albert et al., 2000; Tsartsidou et al., 2007) and up to 44% in South Africa (Esteban et al., 2017). Considering that in our hearth-related samples (C2, C3 and C4) the percentage of Poaceae phytoliths is between 54 and 64.7%, much higher than that observed when they appear as contamination with the wood, we suggest that the presence of grasses in these burning contexts could potentially be related to an intentional use of these plants, probably as tinder.

In square B2, where dicotyledonous phytoliths from wood/bark were more abundant, the FTIR results indicated the presence of diagenetically altered calcitic ash, suggesting that they were part of the fuel residues (ash) generated by combustion processes. The presence of siliceous aggregates in and around the hearths, in samples from Layer B suggests ash dispersion (Table 3). Siliceous aggregates are quite stable and can persist after strong diagenetic processes have occurred (Schiegl et al., 1996). However, the absence of ash-derived calcite in the same samples indicates that calcite has undergone diagenesis, which also explains the absence of ash pseudomorphs. Ash dispersion in cave deposits has been reported in Middle Palaeolithic caves such as Kebara Cave (Israel) and Abrigo de la Quebrada (Spain) (Albert et al., 2000; Esteban et al., 2015).

Dicots fruits could be anthropogenic or natural inputs (e.g., from bird or bat guano input when humans were absent). No abrupt or sustained interruptions in the archaeological deposition regime were identified within Layer B. This, together with the absence of carbonate hydroxylapatite in the sediment makes it less probable that the dicots fruits came from bird or bat droppings (Shahack-Gross et al., 2004). Another possible pathway is through the burning of wood, as fruit trees were part of the local vegetation around the cave. This would involve collecting either green branches with unripe fruit, or dry branches with some fruit still attached, for use as fuel. Along with the presence of phytoliths from dicots fruit, charred seeds from different edible plants from the Fabaceae (*Lens*, *Vicia* and *Lathyrus*), *Ficus,* and *Pistacia* were recovered in Layer B flotation samples, especially from squares A2 and A1. Charred wood from *Quercus* deciduous type, *Pistacia*, and *Amygdalus* were also recovered from these samples (White et al., 2019). Wild legumes and pistachios are important, often dominant components of macrobotanical assemblages from Late Pleistocene archaeological contexts in southwest Asia (Lev et al., 2005; Kabukcu et al., 2021). With additional processing such as heating or soaking to help remove antinutrients, wild legume seeds could have been used for human consumption. Ongoing macrobotanical analyses and future microarchaeological sampling will aim to resolve the question of whether fruits were gathered food resources.

The archaeobotanical data from MHM cave integrates well with preliminary microfaunal data (Stutz et al., 2015), indicating that the site was in an ecotonal setting. At ca. 80 m asl, MHM today is open, dominated by heavily grazed grasses and shrubs. Mediterranean forest prevails to the east, with a transition to oak-dominated vegetation above 400-500 m asl, located several kilometres upslope from MHM (which sits at ca. 80 m asl), toward the Transjordanian Plateau's upland zone, dominated by oak and pine forest. Overall, the macrobotanical results from Layer B at MHM point to a nearby landscape dominated by Mediterranean forest. As noted above, preliminary results on identifications of carbonised seeds and nutshells (White et al., 2019) emphasises the abundance of wild legumes and pistachio shell fragments. This is similar to the results obtained in the late Mousterian context of Kebara Cave (ca. 65-50 ka BP) (Lev et al., 2005; Weiss, 2017), located in the Mediterranean vegetation zone on southern Mt. Carmel. Preliminary examination of wood charcoal from Layer B at MHM also indicates the presence of hardwood species occurring in Mediterranean forest regimes (Stutz et al., 2016). From the undisturbed Layer B phytolith assemblage, the major presence of Poaceae of the C_3 pooid subfamily are indicative of a Mediterranean woodland biome, usually related to more forested vegetation. Multiple lines of evidence point toward Mediterranean woodland substantially closer to the site than is the case today (Stutz and Nilsson Stutz, 2017). Ongoing wood-charcoal analyses and light stable isotope analyses of ungulate tooth enamel may yield more precise vegetation-band reconstructions. A plausible expectation is that, with MIS 3 conditions generally cooler than the present climate, meso-mediterranean vegetation may have extended toward MHM's elevation, at ca. 80 m asl, with supra-mediterranean forest vegetation within a few kilometer's walk uphill. At the same time, the identification of C_4 plant suggest the presence of xerophilic plants, more related to arid environments. On the other hand, in the Jordan Valley palms are related to well-water areas (Bremond et al., 2008), which is consistent with localized wetland environments around springs and seeps at lower elevations, as well as the proximity of the Lake Lisan.

Conclusions

The multi-proxy approach presented here has allowed the identification of different post-depositional processes affecting different areas of the EUP deposits represented by Layer B in the MHM cave. First, modern shepherd disturbance has thoroughly affected the central area of the cave, leading to the formation of Layer A, especially in square B3 and partially the adjacent squares (A1, A2, B2, B4, and B5). Except for parts of square B5, where microfaunal activity has mixed traces of modern dung with Layer B sediments, the eastern and western areas close to the walls of the cave do not show modern disturbance impacts. The archaeological assemblages recovered from these areas represent undisturbed EUP activity areas. Conversely, in the western area of the cave, diagenesis has affected bone preservation, but not that of phytoliths and charred plant macro-remains. The presence of C_3 and C_4 phytoliths in association with other macrobotanical remains indicates that, during the EUP occupation of MHM, wetter areas and Mediterranean woodland vegetation were located near the site, while arid-adapted grasses are also present. The presence of dicot phytoliths and charcoal indicates their use as fuel, alongside grasses, which might be used as tinder. In addition, the presence of siliceous aggregates in and around the hearths suggests ash dispersion. Finally, the concentration of fruit phytoliths, probably of anthropogenic origin, in the western area complements the macrobotanical remains of edible seeds and suggest the incorporation of such plant resources into the diet.

Authors contribution

Mónica Alonso-Eguiluz: Conceptualization, Formal analysis, Investigation, Writing–original draft, Visualization, Writing–review & editing. **Michael B. Toffolo:** Formal analysis, Investigation, Writing–original draft, Visualization, Writing–review & editing. **Chantel E. White:** Writing–review & editing. **Eleni Asouti:** Writing–review & editing. **Elisabetta Boaretto:** Writing–review & editing. **Aaron Stutz**: Project administration, Funding acquisition, Resources, Supervision, Writing–review & editing. **Liv Nilsson Stutz:** Project administration, Funding acquisition, Supervision, Writing–review & editing. **Rosa María Albert**: Conceptualization, Resources, Project administration, Funding acquisition, Supervision, Writing–review & editing.

Acknowledgments

The excavations and research on of MHM have been supported by Oxford College of Emory University; a Gregory-Rackley Career Development Award to A. J. Stutz; NSF High Risk Research in Anthropology Grant (#1025352); the L. S. B. Leakey Foundation; the Wenner-Gren Foundation for Anthropological Research; the MICRO-PAST project funded by the Spanish Ministry of Science and Innovation to RMA (PID2020-119773GB-100); 65 backers of the crowdfunded project, "How Did Palaeolithic Hunter-Gatherers Use and Consume Plant Resources in Eurasia" on Experiment (https://doi.org/10.18258/9109); the Irene Lévi-Sala CARE Foundation; and the American Philosophical Society. We are grateful to the Department of

Antiquities of Jordan. MBT is supported by the grant RYC2021-030917-I, funded by MCIN/AEI/10.13039/501100011033 and by the "European Union NextGenerationEU/PRTR", and wishes to thank Archéosciences Bordeaux for the possibility to use the petrographic microscope to study thin sections at an earlier stage.

References

Albert, R.M., Weiner, S., 2001. Study of phytoliths in prehistoric ash layers from Kebara and Tabun caves using a quantitative approach., in: Meunier, J.D., Colin, F., Faure-Denard, L. (Eds.), Phytoliths, Applications in Earth Science and Human History. Lisse: Balkema, pp. 251–266.

Albert, R.M., Bamford, M.K., Cabanes, D., 2009. Palaeoecological significance of palms at Olduvai Gorge, Tanzania, based on phytolith remains. Quaternary International, 193(1–2), 41–48. https://doi.org/10.1016/j.quaint.2007.06.008

Albert, R.M., Berna, F., Goldberg, P., 2012. Insights on Neanderthal fire use at Kebara Cave (Israel) through high resolution study of prehistoric combustion features: Evidence from phytoliths and thin sections. Quaternary International 247, 278-293. https://doi.org/10.1016/j.quaint.2010.10.016

Albert, R.M., Weiner, S., Bar-Yosef, O., Meignen, L., 2000. Phytoliths in the Middle Palaeolithic deposits of Kebara Cave, Mt Carmel, Israel: Study of the plant materials used for fuel and other purposes. J. Archaeol. Sci., 27(10), 931–947. https://doi.org/10.1006/jasc.2000.0507

Aldeias, V., Dibble, H.L., Sandgath, D., Goldberg, P., McPherron, S.J.P., 2016. How heat alters underlying deposits and implications for archaeological fire features: A controlled experiment. J. Archaeol. Sci. 67, 64-79. https://doi.org/10.1016/j.jas.2016.01.016

Berna, F., Behar, A., Shahack-Gross, R., Berg, J., Boaretto, E., Gilboa, A., Sharon, I., Shalev, S., Shilstein, S., Yahalom-Mack, N., Zorn, J.R., Weiner, S., 2007. Sediments exposed to high temperatures: reconstructing pyrotechnological processes in Late Bronze and Iron Age Strata at Tel Dor (Israel). J. Archaeol. Sci. 34, 358–373. https://doi.org/10.1016/j.jas.2006.05.011

Berna, F., Boaretto, E., Wiebe, M.C., Goder-Goldberger, M., Abulafia, T., Lavi, R., Barzilai, O., Marder, O., Weiner, S., 2021. Site formation processes at Manot Cave, Israel: Interplay between strata accumulation in the occupation area and the talus. Journal of Human Evolution 160, 102883. https://doi.org/10.1016/j.jhevol.2020.102883

Blinnikov, M.S., 2005. Phytoliths in plants and soils of the interior Pacific Northwest, USA. Rev. Palaeobot. Palynol. 135, 71–98. https://doi.org/10.1016/j.revpalbo.2005.02.006

Bremond, L., Alexandre, A., Wooller, M. J., Hély, C., Williamson, D., Schäfer, P. A., Majule, A., Guiot, J., 2008. Phytolith indices as proxies of grass subfamilies on East African tropical mountains. Global and Planetary Change, 61(3–4), 209–224. https://doi.org/10.1016/j.gloplacha.2007.08.016

Cabanes, D., Weiner, S., Shahack-Gross, R. 2011. Stability of phytoliths in the archaeological record: a dissolution study of modern and fossil phytoliths. J. Archaeol. Sci. 38, 2480–2490. https://doi.org/10.1016/j.jas.2011.05.020

Chauhan, D.K., Tripathi, D.K., Kumar, D., Kumar, Y., 2011. Diversity, distribution, and frequency-based attributes of phytolith in Arundo donax L. International Journal of Innovations in Biological and Chemical Sciences 1, 22–27.

Durn, G., Ćorić, R., Tadej, N., Barudžija, U., Rubinić, V., Husnjak, S. 2014. Bulk and clay mineral composition indicate origin of terra rossa soils in Western Herzegovina. Geol. Croat. 67, 171–183. https://doi.org/10.4154/gc.2014.13

Esteban, I., Albert, R.M., Eixea, A., Zilhão, J., Villaverde, V. 2015. Neanderthal use of plants and past vegetation reconstruction at the Middle Paleolithic site of Abrigo de la Quebrada (Chelva, Valencia, Spain). Archaeological and Anthropological Sciences, 9(2), 265–278. https://doi.org/10.1007/s12520-015-0279-7

Esteban, I., Vlok, J., Kotina, E.L., Bamford, M.K., Cowling, R.M., Cabanes, D., Albert, R.M. 2017. Phytoliths in plants from the south coast of the Greater Cape Floristic Region (South Africa). Rev. Palaeobot. Palynol. 245, 69–84. https://doi.org/10.1016/j.revpalbo.2017.05.001

Esteban, I., Bamford, M.K., House, A., Miller, C.S., Neumann, F.H., Schefuß, E., Pargeter, J., Cawthra, H.C., Fisher, E.C., 2020. Coastal palaeoenvironments and hunter-gatherer plant-use at Waterfall Bluff rock shelter in Mpondoland (South Africa) from MIS 3 to the Early Holocene. Quaternary Science Reviews, 250, 106664. https://doi.org/10.1016/j.quascirev.2020.106664

Flügel, E. 2004. Microfacies of carbonate rocks: Analysis, interpretation and application. Springer, Berlin

Fredlund, G.G., Tieszen, L.T., 1994. Modern Phytolith Assemblages from the North American Great Plains. J Biogeogr 21, 321–335. https://doi.org/10.2307/2845533

Goldberg, P., Berna, F., Chazan, M., 2015. Deposition and Diagenesis in the Earlier Stone Age of Wonderwerk Cave, Excavation 1, South Africa. African Archaeological Review 32, 613-643. https://doi.org/10.1007/s10437-015-9192-9

Goldberg, P., Miller, C.E., Schiegl, S., Ligouis, B., Berna, F., Conard, N.J., Wadley, L. 2009. Bedding, hearths and site maintenance in the Middle Stone Age of Sibudu Cave, KwaZulu-Natal, South Africa. Archaeological and Anthropological Sciences 1, 95-122. https://doi.org/10.1007/s12520-009-0008-1

Gur-Arieh, S., Mintz, E., Boaretto, E., Shahack-Gross, R., 2013. An ethnoarchaeological study of cooking installations in rural Uzbekistan: development of a new method for identification of fuel sources. J. Archaeol. Sci. 40, 4331–4347. https://doi.org/10.1016/j.jas.2013.06.001

Kabukcu, C., Asouti, E., Pöllath, N., Peters, J., Karul, N., 2021. Pathways to plant domestication in Southeast Anatolia based on new data from aceramic Neolithic Gusir Höyük. Scientific Reports 11, 2112. https://doi.org/10.1038/s41598-021-81757-9

Karkanas, P., Bar-Yosef, O., Goldberg, P., Weiner, S., 2000. Diagenesis in Prehistoric Caves: the Use of Minerals that Form In Situ to Assess the Completeness of the Archaeological Record. Journal of Archaeological Science 27, 915-929. https://doi.org/10.1006/jasc.1999.0506

Karkanas, P., Rigaud, J.-P., Simek, J.F., Albert, R.M., Weiner, S., 2002. Ash bones and guano: a study of the minerals and phytoliths in the sedimentos of Grotte XVI, Dordogne, France. J. Archaeol. Sci. 29, 721–732. https://doi.org/10.1006/jasc.2001.0742

Katz, O., Cabanes, D., Weiner, S., Maeir, A.M., Boaretto, E., Shahack-Gross, R., 2010. Rapid phytolith extraction for analysis of phytolith concentrations and assemblages during an excavation: an application at Tell es-Safi/Gath, Israel. J. Archaeol. Sci. 37, 1557–1563. https://doi.org/10.1016/j.jas.2010.01.016

Kadowaki, S., Tamura, T., Kida, R., Omori, T., Maher, L. A., Portillo, M., Hirose, M., Suga, E., Massadeh, S., Henry, D. O. (2021). Lithic Technology and Chronology of Initial Upper Paleolithic

Assemblages at Tor Fawaz, Southern Jordan. *Journal of Paleolithic Archaeology*, *5*(1). https://doi.org/10.1007/s41982-021-00107-3

Kehl, M., Burow, C., Cantalejo, P., Domínguez-Bella, S., Durán, J. J., Henselowsky, F., Klasen, N., Linstädter, J., Medianero, J., Pastoors, A., Ramos, J., Reicherter, K., Schmidt, C., Weniger, G. C. (2016). Site formation and chronology of the new Paleolithic site Sima de Las Palomas de Teba, southern Spain. Quaternary Research, 85(2), 313-331. http://dx.doi.org/10.1016/j.yqres.2016.01.007

Lev, E., Kislev, M.E., Bar-Yosef O., 2005. Mousterian vegetal food in Kebara Cave, Mt. Carmel. J. Archaeol. Sci. 32, 475–484. https://doi.org/10.1016/j.jas.2004.11.006

Macphail, R.I., Goldberg, P., 2017. Applied Soils and Micromorphology in Archaeology. Cambridge University Press, Cambridge.

Mercier, N., Valladas, H., Joron, J.L., Schiegl, S., Bar Yosef, O., Weiner, S., 1995. Thermoluminescence Dating and the Problem of Geochemical Evolution of Sediments – A Case Study: The Mousterian Levels at Hayonim. Israel Journal of Chemistry 35, 137-141. https://doi.org/10.1002/ijch.199500021

Mulholland, S.C., Rapp, G., 1992. A Morphological Classification of Grass Silica-Bodies. Phytolith Systematics 65–89. https://doi.org/10.1007/978-1-4899-1155-1_4

Neumann, K., Strömberg, C.A.E., Ball, T., Albert, R.M., Vrydaghs, L., Cummings, L.S., 2019. International Code for Phytolith Nomenclature (ICPN) 2.0. Ann Bot XX, 1–11. https://doi.org/10.1093/aob/mci172

Nicosia, C., Stoops, G., 2017. Archaeological Soil and Sediment Micromorphology. Wiley Blackwell.

Piperno, D., 2006. Phytoliths. A comprehensive guide for archaeologists and paleoecologists. Altamira Press.

Regev, L., Poduska, K.M., Addadi, L., Weiner, S., Boaretto, E., 2010. Distinguishing between calcites formed by different mechanisms using infrared spectrometry: archaeological applications. J. Archaeol. Sci. 37, 3022–3029. https://doi.org/10.1016/j.jas.2010.06.027

Reimer, P., Austin, W., Bard, E., Bayliss, A., Blackwell, P., Bronk Ramsey, C., Butzin, M., Cheng, H., Edwards, R., Friedrich, M., Grootes, P., Guilderson, T., Hajdas, I., Heaton, T., Hogg, A., Hughen, K., Kromer, B., Manning, S., Muscheler, R., Palmer, J., Pearson, C., van der Plicht, J., Reimer, R., Richards, D., Scott, E., Southon, J., Turney, C., Wacker, L., Adolphi, F., Büntgen, U., Capano, M., Fahrni, S., Fogtmann-Schulz, A., Friedrich, R., Köhler, P., Kudsk, S., Miyake, F., Olsen, J., Reinig, F., Sakamoto, M., Sookdeo, A., Talamo, S., 2020. The IntCal20 Northern Hemisphere radiocarbon age calibration curve (0–55 cal kBP). Radiocarbon, 62.

Rodríguez-Cintas, A., Albert, R.M., Bamford, M.K., Stanistreet, I.G., Stollhofen, H., Stone, J.R., Rivera-Rondón, C., Pronzato, R., Njau, J.K., Schick, K., Toth, N., 2020. Palaeovegetation changes recorded in Palaeolake Olduvai OGCP Core 2A (2.09–2.12 Ma) Naibor Soit Formation Olduvai Gorge, Tanzania. Palaeogeogr. Alaeoclimatol. Palaeoecol. 557. https://doi.org/10.1016/j.palaeo.2020.109928

Runge, F. 1999. The opal phytolith inventory of soils in central Africa — quantities, shapes, classification, and spectra. Rev. Palaeobot. Palynol. 107, 23–53.

Schiegl, S., Goldberg, P, Bar-Yosef O, Weiner S (1996) Ash deposits in Hayonim and Kebara Caves, Israel: Macroscopic, microscopic and mineralogical observations, and their archaeological implications. J. Archaeol. Sci. 23, 763–781. https://doi.org/10.1006/jasc.1996.0071

Shahack-Gross, R. 2011. Herbivorous livestock dung: formation, taphonomy, methods for identification, and archaeological significance. J. Archaeol. Sci. 38, 205–218. https://doi.org/10.1016/j.jas.2010.09.019

Shahack-Gross, R., Albert, R.M., Gilboa, A., Nagar-Hilman, O., Sharon, I., Weiner, S., 2005. Geoarchaeology in an urban context: The uses of space in a Phoenician monumental building at Tel Dor (Israel). J. Archaeol. Sci. 32, 1417–1431. https://doi.org/10.1016/j.jas.2005.04.001

Shahack-Gross, R., Berna, F., Karkanas, P., Weiner, S., 2004. Bat guano and preservation of archaeological remains in cave sites. Journal of Archaeological Science 31, 1259-1272. https://doi.org/10.1016/j.jas.2004.02.004

Shakoor, S.A., Soodan, A.S., Kumar, K., 2014. Morphological Diversity and Frequency of Phytolith Types in Gaint Reed Arundo donax (L.). World Appl. Sci. J. 29, 926–932. https://doi.org/10.5829/idosi.wasj.2014.29.07.14

Shea, J.J., Stutz, A.J., Nilsson Stutz, L., 2019. An Early Upper Palaeolithic Stone Tool Assemblage from Mughr El-Hamamah, Jordan: An Interim Report. J. F. Archaeol. 44, 420–439. https://doi.org/10.1080/00934690.2019.1655519

Stoops, G., Marcelino, V., Mees, F., 2018. Interpretation of Micromorphological Features of Soils and Regoliths, Second ed. Elsevier, Oxford.

Stoops, G., 2021. Guidelines for Analysis and Description of Soil and Regolith Thin Sections, Second ed. Wiley.

Stutz, A.J., Shea, J.J., Rech, J. A., Pigati, J.S., Wilson, J., Belmaker, M., Albert, R.M., Arpin, T., Cabanes, D., Clark, J.L., Hartman, G., Hourani, F., White, C.E., Nilsson Stutz, L. 2015. Early Upper Paleolithic chronology in the Levant: new ABOx-SC accelerator mass spectrometry results from the Mughr el-Hamamah Site, Jordan. J. Hum. Evol. 85, 157–173. https://doi.org/10.1016/j.jhevol.2015.04.008

Stutz, A.J., Albert, R.M., Alonso-Eguiluz, M., Arpin, T., Asouti, E., White, C.E., Shea, J.J., Nilsson Stutz, L.G., 2016. Depositional Context of the Early Upper Paleolithic Occupation (45–39 ka) at Mughr el-Hamamah, Jordan: Implications for Tracing Behavioral Change across the Middle-Upper Paleolithic Transition. Presented at the Paleoanthropology Society Annual Meeting, Atlanta.

Stutz, A. J., Nilsson Stutz, L. 2017. Mughr el-Hamamah: An Early Upper Palaeolithic Cave Site on the Eastern Jordan Valley Flanks. Quaternary of the Levant: Environments, Climate Change, and Humans, 285–290.

Taifour, H., El-Oqlah, A., 2016. The plants of Jordan. An annotated checklist, Raffles Bulletin of Zoology Supplement. Key Publishing. Royal Botanic Garden.

Toffolo, M. B., Brink, J. S., van Huyssteen, C., Berna, F., 2017. A microstratigraphic reevaluation of the Florisbad spring site, Free State Province (South Africa): formation processes and paleoenvironment. Geoarchaeology 32 (4), 456-478. https://doi.org/10.1002/gea.21616

Tsartsidou, G., Lev-Yadun, S., Albert, R.M., Miller-Rosen, A., Efstratiou, N., Weiner, S., 2007. The phytolith archaeological record: strengths and weaknesses evaluated based on a quantitative modern reference collection from Greece. J. Archaeol. Sci. 34, 1262–1275. https://doi.org/10.1016/j.jas.2006.10.017

Twiss, P.C., 1992. Predicted world distribution of C3 and C4 grass phytoliths, in: Rapp, G., Mulholland, S.C. (eds). Phytolith Systematics. Emerging Issues. Advances in Archaeological and Museum Science. pp. 113–128.

Vepraskas, M.J., Lindbo, D.L., Stolt, M.H., 2018. Redoximorphic Features. In: Stoops, G., Marcelino, V., Mees, F. (eds) Interpretation of Micromorphological Features of Soils and Regoliths, Second ed. Elsevier, Oxford, pp 425-446.

Weiner, S., 2010. Microarchaeology. Beyond the Visible Archaeological Record. Cambridge University Press, New York.

Weiner, S., Goldberg, P., Bar-Yosef, O., 1993. Bone preservation in Kebara Cave, Israel using on-site fourier transform infrarred spectrometry. J. Archaeol. Sci. 20, 613–627. https://doi.org/10.1006/jasc.1993.1037

Weiner, S., Goldberg, P., Bar-Yosef, O., 2002. Three-dimensional distribution of minerals in the sediments of Hayonim Cave, Israel: Diagenetic processes and archaeological implications. J. Archaeol. Sci. 29, 1289–1308. https://doi.org/10.1006/jasc.2001.0790

Weiner, S., Berna, F., Cohen, I., Shahack-Gross, R., Albert, R.M., Karkanas, P., Meignen, L., Bar-Yosef, O., 2007. Mineral distributions in Kebara Cave: diagenesis and its effect on the archaeological record, in: Bar-Yosef, O., Meignen, L. (Eds.), Kebara Cave, Mt. Carmel, Israel: The Middle and Upper Paleolithic Archaeology, Part 1. Peadoby Museum of Archaeology and Ethnology, Harvard University, Cambridge, MA, pp. 131-146.

Weiss, E., 2017, "Palaeolithic Vegetal Diet in the Southern Levant", in O. Bar-Yosef y Y., Enzel (eds.), Quaternary of the Levant: Environments, Climate Change, and Humans. Cambridge, pp. 329-336. https://doi.org/10.1017/9781316106754.038

White, C., McKain, K., Nilsson Stutz, L., Stutz, A., Asouti, E., 2019. A New Assessment of Macrobotanical Preservation and Recovery: Results from the Early Upper Paleolithic Site of Mughr el-Hamamah, Jordan. American Society of Overseas Research Annual Meeting, San Diego.